Chemical Physics 149 (1991) 275–298
North-Holland

Catastrophes and classical surface scattering

T.C.M. Horn [1], A.W. Kleyn
FOM-Institute for Atomic and Molecular Physics, Kruislaan 407, 1098 SJ Amsterdam, The Netherlands

and

B. Dijkhuis
Centre for Mathematics and Computer Science, P.O. Box 4079, 1009 AB Amsterdam, The Netherlands

Received 29 August 1988; in final form 20 August 1990

Singularities in the intensity distribution for reflection of structureless particles from a massive hard wall are analyzed. This analysis is fully determined by geometrical arguments. The singularities are related to catastrophes from catastrophe theory. In a few examples the potential of a catastrophe analysis as a characterization of the important features of the surface will be shown. For the case of periodical hard wall surfaces, surface scattering, excluding diffraction and energy transfer, is described. Some possible applications of this analysis are discussed. The correspondence between hard wall reflection and hyperthermal atom–surface scattering, including multiple collisions and energy transfer, is used to analyze the catastrophes observed in the latter.

1. Introduction

One of the most general experiments in physics is one where a scattering process is involved. Those experiments are favourite in high-energy physics, nuclear physics, atomic and molecular physics, and in a more recent branch, surface physics. In theory, a scattering process is divided into two well-known states and the unknown, intermediate transformation between those states. In quantum mechanics [1], this is reflected in the formula for the probability p to measure a certain final state Ψ_{final} after preparing the system in the initial state Ψ_{initial}:

$$p = |\langle \Psi_{\text{final}} | \mathbf{S} | \Psi_{\text{initial}} \rangle|^2, \tag{1}$$

where $\mathbf{S}$ stands for the scattering matrix. Consequently, a typical surface scattering experiment consists of the following: a well-characterized beam of particles or light and a well-prepared target as the initial state, and as the final state the well-parameterized detection state and the probability, which most of the time is measured in the form of a differential cross section. In this way it is possible to calculate the scattering matrix $\mathbf{S}$, or, at least, some features of it. After all, all information about the intermediate scattering process is present in the scattering matrix.

In reality, it is hardly ever feasible to determine the states involved completely because in an experiment these states are projected by (implicitly) integrating them inside the machinery. Consequently, a differential cross section is measured with different branches, due to the fact that several initial states end up in the same final state. In the formula for a differential cross section this is represented by the summation over all those initial states. It has been proven that the differential cross section for classical scattering from the initial state $\boldsymbol{a}_n = (a_1, a_2, ..., a_n)$ to the final state $\boldsymbol{A}_n = (A_1, A_2, ..., A_n)$ in the detection point $\boldsymbol{A}_n = \boldsymbol{A}_{n,0}$ is given by [2]

[1] Present address: RAWB, P.O. Box 18524, 2502 EM The Hague, The Netherlands.

$$\sigma(A_{n,0})h(A_{n,0}) = \sigma_{\text{tot}} \sum_i [P(a_n)|J_{n\times n}|^{-1}]_{a_n=a_{n,i}}, \tag{2}$$

where $h(A_{n,0})$ is the Jacobian which represents the transformation from Cartesian coordinates to the coordinates A_n, $P(a_n)$ represents the probability density function for the initial variables and the Jacobian J connects the n-dimensional initial space (a_n) to the n-dimensional final space (A_n), so $J_{n\times n} = |\partial A_n/\partial a_n|$. This has been confirmed, e.g., for classical atom–molecule scattering [3] and for classical atom–surface scattering [4].

Singularities can occur in the mapping from the initial to final state. They appear when the Jacobian J, representing this mapping, vanishes. So, $J=0$ indicates a singularity and gives rise to a so-called rainbow in the intensity distribution, i.e. an infinitesimal region in the detection space where, classically speaking, an infinite intensity can be detected. An extended comment on rainbows in scattering experiments in different branches of physics is given by Kleyn [5]. In surface scattering one-dimensional rainbow curves can be observed [2], which have structures that are characteristic for the azimuthal orientation of the crystal. Classical surface scattering rainbows have, for example, been observed and analyzed by Tenner and co-workers [6–8] and Horn et al. [9].

What does catastrophe theory have to do with rainbow scattering? Catastrophe theory gives a classification of the singularities that can occur in the mapping of one hypersurface to another. This theory, introduced by Thom [10] and very much supported and promoted by Zeeman [11], shows that any singularity is associated to one of the elementary catastrophes. It is worth mentioning that a well-written and understandable introduction to catastrophe theory is given by Poston and Stewart [12]. Concerning our goals, it should be possible to categorize all singularities which are measured and calculated as rainbows in surface scattering. The classification of rainbow singularities can be developed as a tool to assign certain catastrophes to some restricted potential features or certain combinations of catastrophes to some restricted geometrical features of the process. We will call catastrophe analysis the method of analyzing singularities in scattering patterns and relating them to the local topology of the potential energy hypersurface, often reflecting the geometric structure of the surface. This is particularly appropriate, because catastrophes are stable under small distortions like the thermal vibrations of crystal atoms. Related work has already been done, using semiclassical approximations for atom–molecule scattering [13–15], for diffractive scattering [16,17], for semi-classical atom–surface scattering [18], for light scattering by lenses and reflecting surfaces [19,20] [#1], for ion channeling in thin foils [21,22] and for classical hyperthermal atom–surface scattering in two introductionary papers [23,24].

The aim of this paper is to give an introduction to catastrophe analysis in classical surface scattering and to apply it to hyperthermal atom–surface scattering. For simplicity, the introductory part (sections 2–4) will only deal with reflection from surfaces, i.e. scattering without energy exchange. In section 2 the theory behind the catastrophe analysis, which is fully based on geometrical arguments, will be derived. In section 3 the analysis will be made more explicit. Although our derivation is not really new, because its results can also be deduced from the semiclassical theory by Berry [18], it is very instructive to show a simple way to obtain these results for classical scattering. The analysis will be used in section 4 in several calculated examples of reflection. In section 5 some applications of catastrophe analysis will be presented. Finally, in section 6 we will make an analysis for hyperthermal atom–surface scattering including energy transfer of the projectile to the solid.

2. Derivation of the intensity distribution

Reflection from simple hard wall surfaces can give rise to caustics, i.e. curves of high intensity, which are associated with elementary catastrophes. Using sinusoidal hard walls, this has been shown by Berry [18] and Horn and co-workers [4,23,24]. In this paper we will derive from first principles a way to distinguish fold, cusp and umbilic catastrophes, occurring in reflection experiments. Of course, catastrophe theory gives a direct method

[#1] The authors like to thank M.V. Berry for bringing ref. [20] to their attention.

to determine the kind of singularity, but most of the time it is hard to do and quite time consuming.

In the following derivation we have in mind a scattering experiment in which a beam of particles impinges on a crystal surface and the reflected particles are detected at a screen placed at some distance of the crystal perpendicular to the incoming beam. We want to derive a formula for the intensity distribution at that screen. In order to facilitate the calculations we make the following idealizations and simplifications:

(a) The reflection is treated classically, as if the particles are balls bouncing off a hard wall. Diffraction is not taken into account.

(b) There is no recoil of the surface so that no energy exchange is considered.

(c) There are no multiple collisions; this requires that the corrugation of the crystal surface is small. The angle of inclination of the slopes must remain well below 45°. In an experimental situation, it is not trivial to accomplish this condition. In section 5 we will come back to this experimental problem.

The situation can be described as follows. A Cartesian coordinate system is chosen such that the incoming particles move parallel to the z-axis in the direction of negative z. The hard wall is described by the height function $z=f(x, y)$. The detection screen is assumed to be placed at a fixed distance $z=C$ parallel to the xy-plane. Positions on this screen are denoted by the capitals (X, Y). A schematic drawing, showing the variables used, is given in fig. 1.

When a beam of particles is reflected from the hard wall surface $z=f(x, y)$ the image on a distant detection screen will expose singularities in the intensity distribution. We shall calculate the function $I=I(X, Y)$ analytically, using only simple geometrical arguments.

Now consider a particle that hits the surface at the point $(x, y, f(x, y))$ (see fig. 1). The normal to the surface at this point is given by the vector

$$\boldsymbol{n}=\frac{1}{\sqrt{f_x^2+f_y^2+1}}\begin{pmatrix}-f_x\\-f_y\\1\end{pmatrix}. \tag{3}$$

The angle α between this normal and the z-axis satisfies the relation

$$\tan\alpha=\sqrt{f_x^2+f_y^2}\,, \tag{4}$$

while the angle β between the projection of $\boldsymbol{n}$ on the x, y-plane and the x-axis is determined by

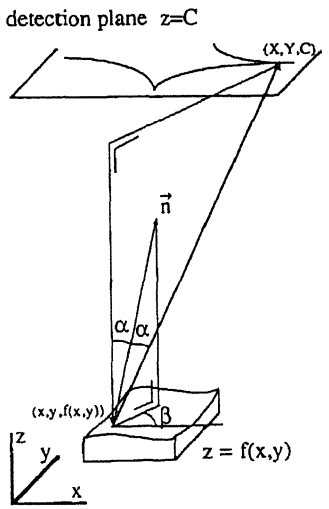

Fig. 1. A schematic view of the system, used in the derivation of classification conditions for the appearance of fold, cusp and umbilic catastrophes in reflection calculations from corrugated hard walls. In the coordinate system (x, y, z) the hard wall height function $z=f(x, y)$ is embedded. The observation (detection) screen is placed parallel to the xy-plane at the plane $z=C$. Points on the screen are denoted by (X, Y). Furthermore, the definition of the polar angle α and the azimuthal angle β is shown.

$$\tan\beta=\frac{f_y}{f_x}. \tag{5}$$

By the law of reflection the reflected particle moves in the plane through the incident direction and the normal n, in such a way that the incident and outgoing directions make equal angles with the normal. Since the incident direction is parallel to the z-axis, it follows that the angles of the outgoing trajectory are given by $(2\alpha, \beta)$. Consequently, the reflected particle will hit the screen placed in the plane $z=C$ at the point (X, Y, C), where (see fig. 1)

$$X=X(x,y)=x+[C-f(x,y)]\tan 2\alpha\cos\beta=x-\frac{2[C-f(x,y)]f_x}{1-f_x^2-f_y^2}, \tag{6a}$$

$$Y=Y(x,y)=y+[C-f(x,y)]\tan 2\alpha\sin\beta=y-\frac{2[C-f(x,y)]f_y}{1-f_x^2-f_y^2}. \tag{6b}$$

Here we have used eqs. (4) and (5), and the goniometric formula $\tan 2\alpha=2\tan\alpha/(1-\tan^2\alpha)$.

In order to determine the intensity distribution I of the reflected particles at the screen, we consider all particles that are reflected from a small surface element Δs near the point $(x_0, y_0, z_0=f(x_0, y_0))$. This surface element is chosen such that its projection on the (x, y)-plane is a rectangle with corners (x_0, y_0), $(x_1=x_0+\Delta x, y_1=y_0)$, $(x_2=x_0+\Delta x, y_2=y_0+\Delta y)$, $(x_3=x_0, y_3=y_0+\Delta y)$. The particles reflected from this surface element will hit the screen in a region bounded by the lines connecting the corners (X_i, Y_i), $i=0, 1, 2, 3$. For small Δx and Δy this region is approximately (in first order in Δx and Δy) a parallelogram with area equal to:

$$\Delta S=\begin{vmatrix} X_1-X_0 & Y_1-Y_0 \\ X_3-X_0 & Y_3-Y_0 \end{vmatrix}\approx\begin{vmatrix} X_x & Y_x \\ X_y & Y_y \end{vmatrix}_{(x_0,y_0)}\Delta x\,\Delta y=J_{(x_0,y_0)}\Delta x\,\Delta y, \tag{7}$$

where $J=|\partial(X, Y)/\partial(x, y)|$ is the Jacobian of the transformation in eq. (6) from the space of impact parameters (x, y) to the space of detection given by the position (X, Y) on the screen.

By differentiating X and Y in eqs. (6) with respect to x and y, we find after a long calculation including a great part of bookkeeping, that the Jacobian can be written as:

$$J_{(x_0,y_0)}=AQ^2\left|\frac{1}{Q^2}-\frac{\nabla^2 f(x_0,y_0)}{Q}+H[f(x_0,y_0)]\right|, \tag{8}$$

where $\nabla^2 f(x, y)=f_{xx}+f_{yy}$ is the Laplacian, $H[f(x, y)]=f_{xx}f_{yy}-f_{xy}^2$ is the Hessian of the function $f(x, y)$, and Q and A are given by

$$Q=\frac{2[C-f(x,y)]}{1-f_x^2-f_y^2} \tag{9}$$

and

$$A=\frac{1+f_x^2+f_y^2}{1-f_x^2-f_y^2}, \tag{10}$$

evaluated at $x=x_0$ and $y=y_0$.

If ϕ_0 is the flux (particles/cm^2 s) of the incoming particles through a plane parallel to the xy-plane, then the number N of particles per second that reflects at the surface element Δs and, subsequently, hits the screen within the region ΔS is equal to:

$$N=\phi_0\Delta x\Delta y. \tag{11}$$

Hence, the intensity I on the screen near the point (X_0, Y_0) is given by

$$I(X_0, Y_0) = \frac{N}{\Delta S} = \phi_0 |J|^{-1}_{(x_0, y_0)} . \tag{12}$$

From this equation it follows that singularities in the intensity distribution on the screen will appear when the Jacobian vanishes. This will occur, as we see from eq. (8), if $1/Q$ is a root of the quadratic equation in $1/Q$:

$$\frac{1}{Q_\pm} = \tfrac{1}{2}(f_{xx} + f_{yy}) \pm \sqrt{\tfrac{1}{4}(f_{xx} - f_{yy})^2 + f_{xy}^2} . \tag{13}$$

Singularities of this type are traditionally called rainbows (see, e.g., refs. [2,4,5]). In this paper we will classify those rainbows as catastrophes of different order according to catastrophe theory. Why such singularities can occur is now easily understood. We have seen that the small region Δs on the surface is approximately transformed by reflection into a parallelogram ΔS on the screen. According to eq. (7) the area of this parallelogram is proportional to the Jacobian. So, if the Jacobian vanishes the area of the parallelogram is equal to zero. Consequently, the intensity measured on the screen at that place becomes infinite, giving rise to so-called caustics, named after the bright spots in light scattering [11,12,18–20]. There are two ways by which the area of the parallelogram can become zero. Firstly, the four sides can pairwise coalesce, reducing the parallelogram to a line interval. This gives the lowest order singularity, which in catastrophe theory is called a fold catastrophe. Secondly, the parallelogram can even shrink into a single point. Obviously, the singularity is in this case of higher order. Later we will see that this singularity is a cusp or an umbilic catastrophe.

The intensity distribution in eq. (12) results from the particles reflected from a single surface element Δs near the point (x_0, y_0). However, there may be yet other surface elements from which the particles are reflected into the same region ΔS at the screen. The total intensity will be the sum of the contributions of all those surface elements. Hence, the total intensity is given by

$$I(X_0, Y_0) = \sum_i \phi_0 |J|^{-1}_{(x_i, y_i)} , \tag{14}$$

where (x_i, y_i) are the coordinates of those points on the hard wall that reflect to the same point (X_0, Y_0) on the screen. This is the general formula for the intensity distribution on a detection screen in the (x, Y)-plane at $z = C$ for reflection of structureless particles from a hard wall given by the hard wall height function $z = f(X, y)$.

Up to now we have considered the situation where the screen is at a finite distance from the reflecting surface. We note, however, that in most scattering experiments the detection screen is at a distance from the surface which is very large with respect to the size of the reflecting sample. For that reason we consider here an idealized experiment in which the screen is at infinity. Since for a screen at infinity the coordinates X and Y are useless, we introduce normalized screen coordinates:

$$(X^*, Y^*) = \lim_{C \to \infty} (X/C, Y/C) . \tag{15}$$

From eq. (6) it follows, by letting $C \to \infty$, that the position where the reflected particle hits the screen is given by

$$(X^*, Y^*) = (-2f_x/(1 - f_x^2 - f_y^2) , -2f_y/(1 - f_x^2 - f_y^2)) . \tag{16}$$

Correspondingly, we define a normalized asymptotic intensity distribution function I^* by

$$I^*(X_0^*, Y_0^*) = \lim_{C \to \infty} C^2 I(CX_0^*, CY_0^*) . \tag{17}$$

From eqs. (8) and (14) we then find

$$I^*(X_0^*, Y_0^*) = \sum_i B_i |H(f(x_i, y_i))|^{-1} , \tag{18}$$

where

$$B_i = \phi_0 \frac{(1-f_x^2-f_y^2)^3}{4(1+f_x^2+f_y^2)} \tag{19}$$

evaluated at $(x, y)=(x_i, y_i)$.

Eq. (18) gives the general result for the normalized intensity distribution at infinity for reflection of structureless particles from hard wall surfaces. The differential cross section σ can now be calculated by a spherical transformation of the Euclidian coordinates into polar coordinates (R, ϑ, φ). The result in eq. (18) is in agreement with an earlier derivation of the differential cross section for reflection from a hard wall by calculating the Jacobian $J=|\partial(\vartheta, \varphi)/\partial(x, y)|$ using the evaluation of the derivatives of the final variables ϑ and φ with respect to the initial variables x and y [4]. The summation in eq. (18) corresponds to the characteristic branches of the differential cross section in surface scattering [2]. Now, considering the intensity distribution at infinity, this summation can have different origins. As we have already mentioned, different regions Δs on the hard wall surface will accidently reflect to the same region ΔS on the screen. In case of periodical hard wall surfaces the summation will also run over all unit cells in the sample.

Let us now sketch the procedure which we shall use to analyze the reflection examples to be discussed. Eq. (18) shows that the singularities in the reflected intensity on the screen will occur when the Hessian vanishes. By solving the identity $H[f(x, y)]=0$, either analytically or numerically, it is possible to calculate the set of impact parameters which will by reflection transform into the caustics. We shall call the $H=0$ contours the origin curves of the caustics. Subsequently, we will then relate these origin curves with the behaviour of the final variables X and Y with respect to the impact parameters x and y, from which we can already roughly deduce the order of singularity. The Jacobian in eq. (7) contains the derivatives of the two independent final variables X and Y with respect to the initial variables x and y. The simplest way to get a vanishing Jacobian is when one of the two final variables is stationary. Furthermore, both rows or columns can be dependent, also giving rise to a zero Jacobian. This is extensively discussed in ref. [4]. In all these cases fold catastrophes will appear on the screen because the parallelogram becomes a line interval after reflection. But, in case that the second final variable also meets an extremum at the same initial point (x, y), all elements of the Jacobian are equal to zero. Later on we will see that this corresponds to an umbilic catastrophe. In the examples of reflection from periodical corrugated hard walls we will use these phenomena by considering the extrema or saddle points in the final angles ϑ and φ.

3. Caustics at infinity

We will analyze the caustics at infinity in more detail in this section. Before we do so, we shall further simplify the formulae for the mapping in eq. (16). It turns out that it is possible to get rid of the denominator in these expressions by employing a little trick, which will presently be explained. In terms of the polar angles (α, β) of the normal $\boldsymbol{n}$ to the surface (cf. eqs. (4) and (5)), the mapping in eq. (16) can be rewritten as

$$(X^*, Y^*)=(-\tan 2\alpha \cos\beta, -\tan 2\alpha \sin\beta)\,. \tag{20}$$

The doubling of the angle α is, as we recall, a consequence of the law of reflection. Without doubling, we would have obtained the much simpler mapping:

$$(X^{**}, Y^{**})=(-\tan\alpha\cos\beta, -\tan\alpha\sin\beta)=(-f_x, -f_y)\,. \tag{21}$$

Actually, the point (X^{**}, Y^{**}) corresponds to the direction of the normal to the surface. The relation between (X^*, Y^*) and (X^{**}, Y^{**}) is given by

$$(X^*, Y^*)=(2X^{**}/(1-X^{**2}-Y^{**2}), 2Y^{**}/(1-X^{**2}-Y^{**2}))\,, \tag{22}$$

with the inverse

$$(X^{**}, Y^{**}) = (X^*(\sqrt{1+X^{*2}+Y^{*2}}-1)/(X^{*2}+Y^{*2}),\ Y^*(\sqrt{1+X^{*2}+Y^{*2}}-1)/(X^{*2}+Y^{*2})) . \tag{23}$$

Note that the mapping $(X^*, Y^*) \to (X^{**}, Y^{**})$ induced by the transition from 2α to α is a pure radial contraction in the direction of the origin. Moreover, it is a very smooth contraction. Therefore, a smooth curve in the (X^*, Y^*)-plane will be transformed into a smooth curve in the (X^{**}, Y^{**})-plane with roughly the same shape, while irregularities will be transformed into irregularities of the same kind. Since the formulas become much simpler if we work with the mapping in eq. (21) instead of eq. (16), we shall henceforth base our further analysis on the (X^{**}, Y^{**})-representation. Any result obtained in this way can easily be expressed in (X^*, Y^*)-coordinates by using the transformation given in eq. (23).

Now, we shall investigate in more detail the shape of the caustics, or rather the shape of the curve in the (X^{**}, Y^{**})-plane which is the image of the caustic under the contraction in eq. (23). From the preceding section we known that a caustic at infinity results from reflection in the point where the Hessian of the hard wall height function $z=f(x, y)$ vanishes. Therefore, we first look at the zero-contour of $H[f(x, y)]$. Let us assume that the zero-contour has a parameter representation $r=r(t)=(x(t), y(t))$, where x and y are differentiable functions of the parameter t on the interval (a, b). From the condition $H[f(x(t), y(t))]=0$ for all $t\in(a, b)$ it follows that

$$0=\frac{dH}{dt}=\frac{\partial H}{\partial x}\frac{dx}{dt}+\frac{\partial H}{\partial y}\frac{dy}{dt}. \tag{24}$$

Hence, the direction of the tangent to the zero-contour in the point $(x(t), y(t))$ is given by

$$\frac{dy}{dx}=\frac{dy/dt}{dx/dt}=-\frac{\partial H/\partial x}{\partial H/\partial y}=-\frac{f_{xx}f_{xyy}+f_{yy}f_{xxx}-2f_{xy}f_{xxy}}{f_{xx}f_{yyy}+f_{yy}f_{xxy}-2f_{xy}f_{xyy}}. \tag{25}$$

Since the contracted caustic curve is the image of the zero-contour under the mapping in eq. (21), it has the parameter representation:

$$\boldsymbol{R}=\boldsymbol{R}(t)=(X^{**}(t), Y^{**}(t))=(-f_x(x(t), y(t)), -f_y(x(t), y(t))) . \tag{26}$$

Thus, the derivatives of X^{**} and Y^{**} with respect to t are given by

$$\frac{dX^{**}}{dt}=-f_{xx}\frac{dx}{dt}-f_{xy}\frac{dy}{dt},\quad \frac{dY^{**}}{dt}=-f_{xy}\frac{dx}{dt}-f_{yy}\frac{dy}{dt}. \tag{27}$$

It is instructive to rewrite these equations in matrix form. Let $d\boldsymbol{r}=\mathrm{col}(dx, dy)$ denote the displacement along the zero-contour caused by a change dt in the parameter t, and let $d\boldsymbol{R}=\mathrm{col}(dX^{**}, dY^{**})$ be the corresponding displacement along the contracted caustic. Then the pair of equations (27) can be rewritten in matrix form as:

$$d\boldsymbol{R}=-\mathbf{M}\,d\boldsymbol{r}=-\begin{pmatrix} f_{xx} & f_{xy} \\ f_{xy} & f_{yy} \end{pmatrix}\begin{pmatrix} dx \\ dy \end{pmatrix}. \tag{28}$$

Because $\mathbf{M}$ is a symmetric matrix, it has the following properties:

(a) The two eigenvalues of $\mathbf{M}$, denoted by λ_i and λ_j, are real.

(b) The corresponding normalized eigenvectors $\boldsymbol{i}$ and $\boldsymbol{j}$ are perpendicular if $\lambda_i\neq\lambda_j$, or, they can be chosen so if $\lambda_i=\lambda_j$, i.e. $|\boldsymbol{i}|=|\boldsymbol{j}|=1$ and $\boldsymbol{i}\cdot\boldsymbol{j}=0$.

(c) The sum of the eigenvalues is equal to the trace of the matrix $\mathbf{M}$, while their product is equal to the determinant of the matrix $\mathbf{M}$.

If we are on the zero-contour of $H=H[f(x, y)]$, then the last statement implies that at least one of the eigenvalues, let us say λ_i, is equal to zero, so that $\lambda_i=0$ and $\lambda_j=f_{xx}+f_{yy}$. Using the decomposition $d\boldsymbol{r}=(\boldsymbol{i}\cdot d\boldsymbol{r})\boldsymbol{i}+(\boldsymbol{j}\cdot d\boldsymbol{r})\boldsymbol{j}$ and the properties $\mathbf{M}\boldsymbol{i}=\lambda_i\boldsymbol{i}=0$, $\mathbf{M}\boldsymbol{j}=\lambda_j\boldsymbol{j}$, we obtain from eq. (28):

$$d\boldsymbol{R} = -\lambda_j (\boldsymbol{j} \cdot d\boldsymbol{r}) \boldsymbol{j} . \tag{29}$$

Thus, in each point of the contracted caustic curve the tangent is parallel to the eigenvector $\boldsymbol{j}$ belonging to the non-zero eigenvalue of $\mathbf{M}$, i.e. parallel to the direction of the strongest curvature of the surface in the corresponding impact point.

The formula in eq. (29) has a nice physical interpretation. This follows from the fact that the directions of the eigenvectors $\boldsymbol{i}$ and $\boldsymbol{j}$ of $\mathbf{M}$ are precisely those directions in which the curvature of the surface is extremal. The eigenvalue is equal to the second derivative taken in the direction of the corresponding eigenvector. The fact that $\lambda_i = 0$ on the zero-contour of $H[f(x, y)]$ implies that at the points of the zero-contour the surface has no curvature in the direction given by the eigenvector $\boldsymbol{i}$. Therefore, in such a point the surface locally has the shape of a cylindrical surface with its axis of revolution parallel to the vector $\boldsymbol{i}$. When we move in the $\boldsymbol{i}$-direction along the surface the normal to the surface keeps the same direction. Consequently, the particles that hit the surface in neighbouring impact points along that $\boldsymbol{i}$-direction are all reflected into the same outgoing direction. This results in a focusing at infinity that produces the caustic. On the other hand, if we move in the $\boldsymbol{j}$-direction, the surface curves. Hence, the direction of the normal changes and for that reason the focusing point also moves in a direction perpendicular to the vector $\boldsymbol{i}$. This explains why in eq. (29) $d\boldsymbol{R}$ has the direction of $\boldsymbol{j}$.

When we move along the Hessian's zero-contour the values of $f(x, y)$ and its higher order derivatives change, in general. Hence, not only the direction of $d\boldsymbol{r}$ but also the directions of the eigenvectors $\boldsymbol{i}$ and $\boldsymbol{j}$ of $\mathbf{M}$ vary with t. If $f(x, y)$ is at least three times continuously differentiable, this is a continuous change. Since $\boldsymbol{j}$ and $d\boldsymbol{r}$ vary to a certain extend independently, it may happen that at a certain point of the zero-contour $\boldsymbol{j}$ is perpendicular to $d\boldsymbol{r}$, which means that $\boldsymbol{j} \cdot d\boldsymbol{r} = 0$. Typically, $\boldsymbol{j} \cdot d\boldsymbol{r}$ will have opposite signs at both sides of this point. From eq. (29) it then follows that the direction of $d\boldsymbol{R}$ changes abruptly at such a point from parallel to anti-parallel to $\boldsymbol{j}$ or vice versa. As a consequence the caustic shows a cusp at this point. For obvious reasons this type of singularity is called a cusp catastrophe.

Note that on account of eq. (27) the condition $d\boldsymbol{R} = 0$ is equivalent to the conditions:

$$f_{xx}\, dx + f_{xy}\, dy = f_{xy}\, dx + f_{yy}\, dy = 0 . \tag{30}$$

When we move along the zero-contour towards the point where eq. (30) holds, the image point moves along the contracted caustic with diminishing speed, then stops at the cusp point and subsequently turns back. As a consequence, the singularity in the intensity distribution is of higher order than in the case of the simple fold catastrophe.

Another type of singularity occurs when λ_j vanishes at some point of the zero-contour, so that both eigenvalues of $\mathbf{M}$ are equal to zero. From $\lambda_j = f_{xx} + f_{yy} = 0$ it follows that $H[f(x, y)] = -f_{xx}^2 - f_{xy}^2$ and, hence, from $H = 0$:

$$f_{xx} = f_{yy} = f_{xy} = 0 . \tag{31}$$

A point on the surface where the height function $f(x, y)$ has this property is called an umbilic point. In such a point the surface is locally flat, so that in a small neighbourhood of that point the normals to the surface all have (approximately) the same direction. Because of that, the particles reflected from that area on the hard wall surface all hit the screen in the same spot and, therefore, produce a very bright spot.

A consequence of the property given in eq. (31) is that eq. (25) cannot be used to determine the direction of the zero-contour at an umbilic point, because both numerator and denominator of that expression vanish at that point. In order to find the direction of the zero-contour at an umbilic point we have to look at the second derivative of the Hessian with respect to t. Since $H[f(x, y)]$ is constant (equal to zero) along the zero-contour we have

$$0 = \frac{d^2 H}{dt^2} = \frac{\partial^2 H}{\partial x^2}\left(\frac{dx}{dt}\right)^2 + 2\frac{\partial^2 H}{\partial x\, \partial y}\frac{dx}{dt}\frac{dy}{dt} + \frac{\partial^2 H}{\partial y^2}\left(\frac{dy}{dt}\right)^2 . \tag{32}$$

Working out the second derivatives of the Hessian with the condition of eq. (31) taken into account, we can rewrite eq. (32) as a quadratic equation in dy/dx of the form:

$$(f_{xxy}f_{yyy}-f_{xyy}^2)\left(\frac{dy}{dx}\right)^2+(f_{xxx}f_{yyy}-f_{xxy}f_{xyy})\frac{dy}{dx}+(f_{xxx}f_{xyy}-f_{xxy}^2)=0\,. \tag{33}$$

Whether this equation has a real solution or not depends on the sign of the discriminant Γ:

$$\Gamma=\Gamma(f_{xxx},f_{xxy},f_{xyy},f_{yyy})=(f_{xxx}f_{yyy}-f_{xxy}f_{xyy})^2-4(f_{xxy}f_{yyy}-f_{xyy}^2)(f_{xxx}f_{xyy}-f_{xxy}^2)\,. \tag{34}$$

We shall call the umbilic point hyperbolic if $\Gamma>0$, parabolic if $\Gamma=0$ and elliptic if $\Gamma<0$. This classification of umbilic points is the same as the one made by Berry and Hannay [25], except that our discriminant is defined having the opposite sign.

If $\Gamma>0$ there are two different real solutions of eq. (33). This means that in a hyperbolic point of the surface two branches of the zero-contour intersect each other. Consequently, at the screen there will be a confluence of two caustic lines, ideally two cusps with a common vertex. If $\Gamma=0$ the equation has two equal real solutions. In a parabolic umbilic point therefore the two branches of the zero-contour touch each other. Their images coalesce in the neighbourhood of their common vertex. Finally, if $\Gamma<0$ there are no real solutions of eq. (33). Hence, there is no zero-contour of the Hessian passing through an elliptic umbilic point. On the screen at infinity the singularity is just an isolated point with infinite intensity.

Summarizing, we have found three conditions for the occurrence of catastrophes on a distant screen in hard wall reflection. Those conditions belong to different orders of catastrophes. A caustic appears when

$$H[f(x,y)]=f_{xx}f_{yy}-f_{xy}^2=0\,. \tag{35a}$$

This caustic curve will in general be a set of fold catastrophes. On a fold curve a cusp catastrophe appears when, in addition, the following condition is valid:

$$\boldsymbol{j}\cdot d\boldsymbol{r}=f_{xx}\,dx+f_{xy}\,dy=f_{xy}\,dx+f_{yy}\,dy=0\,. \tag{35b}$$

A higher order catastrophe, an umbilic, occurs if all second derivatives vanish:

$$f_{xx}=f_{yy}=f_{xy}=0\,. \tag{35c}$$

4. Reflection calculations from hard wall surfaces

In this section we will apply the foregoing classification to some selected examples of hard wall reflection calculations. We will focus on the change of the reflection patterns, and in particular the singularities thereof, that result from the change of shape of the reflecting surfaces. The goal of this section is to show in what way the occurrence of catastrophes in the reflection pattern is related to the main surface characteristics.

A convenient set of surfaces for examining the relation between the shape of the reflecting surface and the catastrophes in the reflection pattern is provided by the family of ondulating surfaces described by the height function:

$$z=f(x,y,p,q)=A(p+\cos x)(q+\cos y)\,. \tag{36}$$

Here p and q are adjustable parameters which determine the shape of the surface. The amplitude A must be chosen such that the angle of inclination remains well below 45°. Most members of this family produce caustics with cusps. But some of them produce umbilics as well, which may be of the hyperbolic, elliptic or parabolic type. By varying p and q we can shown how the caustics are transformed when the shape of the reflecting surface is altered.

A major advantage of using the function f of eq. (36) lies in the fact that most quantities needed in the analysis can be calculated analytically. Differentiating f repeatedly with respect to x and y we obtain:

$$f_x = -A \sin x\,(q+\cos y)\,, \quad f_y = -A(p+\cos x)\sin y\,, \tag{37}$$

$$f_{xx} = -A\cos x(q+\cos y)\,, \quad f_{xy} = A\sin x \sin y\,, \quad f_{yy} = -A(p+\cos x)\cos y\,, \tag{38}$$

$$f_{xxx} = -f_x\,, \quad f_{xxy} = A\cos x \sin y\,, \quad f_{xyy} = A\sin x \cos y\,, \quad f_{yyy} = -f_y\,. \tag{39}$$

For the Hessian we find after applying some trigoniometric identities:

$$H[f] = A^2(p\cos x\cos^2 y + q\cos^2 x\cos y + pq\cos x\cos y + \cos^2 x + \cos^2 y - 1)\,. \tag{40}$$

This expression is quadratic in $\cos x$ and in $\cos y$, so that the zero-contours can easily be calculated. We will give explicit formulas when we discuss specific examples.

The Hessian $H[f]$ is, just like f, not only 2π-periodic in x and y, but also symmetric in x and y. Therefore, the zero-contours are symmetric with respect to the lines $x = k\pi$ and to the lines $y = k\pi$, $k = 0, \pm 1, \ldots$ The same symmetry holds for the special points lying on these contours, such as umbilics or cusp-producing points. Thus, if (x_0, y_0) is a point with such a special property, then all points with coordinates $(\pm x_0 + 2k\pi, \pm y_0 + 2m\pi)$, where $k, m = 0, \pm 1, \pm 2, \ldots$, have the same property. Since it is rather cumbersome to list each time the whole set of points that have a certain property, we will in this section usually mention only the representant lying in the subsquare $0 \leqslant x_0, y_0 \leqslant \pi$. Note, however, that opposite points such as (x_0, y_0) and $(x_0, -y_0)$, where $\sin y_0 \neq 0$, correspond to two different points on the screen, which lie symmetric with respect to the screen X-axis, as follows from eqs. (37) and (16). Similarly, the pairs (x_0, y_0) and $(-x_0, y_0)$ correspond to screen points which are symmetric with respect to the Y-axis. When we want to stress this type of symmetry as, e.g., in table 1, we will list all equivalent points in the larger square $0 \leqslant x, y \leqslant 2\pi$ which corresponds to the unit cell.

We will now investigate under what circumstances singularities do occur. In section 3 we have found that an umbilic point appears when all second derivatives of f vanish at some point (x_0, y_0). It is easily deduced from eq. (38) that this can occur only if p or q is equal to 0, 1 or -1. In table 1 we list the umbilics that are present for the cases $q = 0, 1, -1$, with the coordinates (x_0, y_0) of the impact points, the values f_x and f_y in that point and the value of the discriminant Γ defined in eq. (34). It appears that Γ can be positive, negative or zero, depending on the value of p and q, so that indeed all types of umbilics can occur within the family given by eq. (36).

The corresponding data of the umbilics that occur in cases $p = 0$, 1, or -1 can be obtained from table 1 by interchanging the entries for x_0 and y_0 and for f_x and f_y simultaneously with p and q. This is a consequence of the function f in eq. (36) being invariant if x and y are interchanged together with p and q.

Another symmetry is associated with the sign reversal of p and q. This is due to the fact that if p is replaced by $-p$ and, simultaneously, x by $\pi - x$ in eq. (36), then the function f simply changes sign. But f and $-f$ have the same Hessian and, therefore, the same zero-contours. The reflection pattern, however, is inverted because both f_x and f_y change sign with f. As a consequence, the replacement of p and $-p$ in the height function f results in

Table 1
Occurrence of umbilics in the reflection from the hard wall surfaces given by eq. (36)

p	q	x_0	y_0	f_x	f_y	Γ
p	0	0	$\pi/2$	0	$-A(1+p)$	$4A^4(1+p)$
		0	$3\pi/2$	0	$A(1+p)$	$4A^4(1+p)$
		π	$\pi/2$	0	$A(1-p)$	$4A^4(1-p)$
		π	$3\pi/2$	0	$-A(1-p)$	$4A^4(1-p)$
$0 < \lvert p\rvert < 1$	1	$\pi \pm \arccos p$	π	0	0	0
$0 < \lvert p\rvert < 1$	-1	$\pi \pm \arccos p$	0	0	0	0

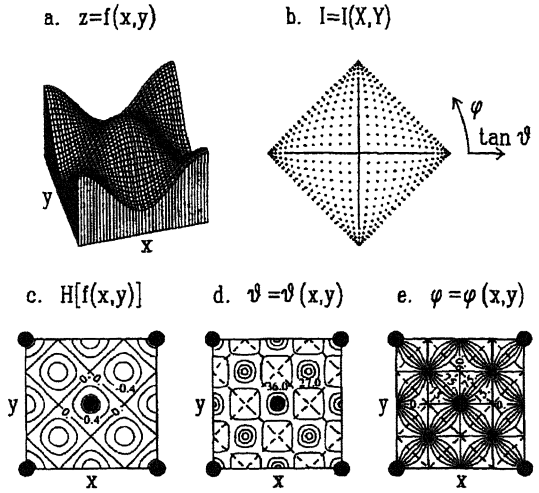

Fig. 2. Results of a reflection calculation from a periodical, corrugated hard wall, described by the hard wall height function $z=f(x, y)=0.1 \cos x \cos y$. The following plots are drawn: (a) A 3-dimensional view of the unit cell of the hard wall height function $z=f(x, y)$ as a function of the 2-dimensional impact parameter $b=(x, y)$. (b) The reflection pattern on the detection screen at infinity. The plot shows a polar diagram of the intensity distribution $I=I(X, Y)$, which is proportional to the density of points, while X and Y relates to ϑ and φ via $(X, Y)=(\tan\vartheta\cos\varphi, \tan\vartheta\sin\varphi)$. (c) A topographical plot (i.e. contour representation) of the Hessian $H[f(x, y)]$ of the hard wall height function $z=f(x, y)$ as a function of the impact parameter (x, y). (d) A topographical plot of the polar angle ϑ as a function of the impact parameter (x, y), where the dotted curve represents the Hessian's zero-contour. (e) A topographical plot of the azimuthal angle φ as a function of the impact parameter (x, y), where the dotted curve represents the Hessian's zero-contour. For convenience, the azimuthal angle has been mapped into the range $\langle 0°, 90°\rangle$.

reflecting the zero-contours with respect to the line $x=\pi/2$ and inverting the reflection pattern on the screen. Analogously, replacement of q by $-q$ causes the zero-contours to be reflected in the line $y=\pi/2$ and the reflection pattern to be inverted, too. For those reasons, it suffices to investigate the function with non-negative p and q, as we will do in the sequel.

In the following we will discuss some pertinent examples of high order singularities in scattering from cosine-shaped, periodical hard wall surfaces. We start by investigating the case $p=q=0$. A perspective view of the hard wall surface $f=A\cos x\cos y$ is drawn in fig. 2a (where we have exaggerated the vertical dimension in order to provide a nice 3D view). A simulation of the reflection pattern is plotted in fig. 2b. This plot is obtained by laying a grid of points over the square $0\leqslant x, y\leqslant 2\pi$ and by calculating for each grid point the position at which a particle reflected at the corresponding impact point on the hard wall surface would hit the screen at infinity according to eq. (16). The resulting reflection pattern for $A=0.1$ is almost a square with sides curved slightly inwards. (The curvature would have been more pronounced if we had chosen a larger value than 0.1 for the amplitude A). The caustics are at the boundaries of the pattern.

If $p=q=0$ the Hessian reduces to $H=A^2(\cos^2 x-\sin^2 y)$. A contourplot of this H is shown in fig. 2c. The zero-

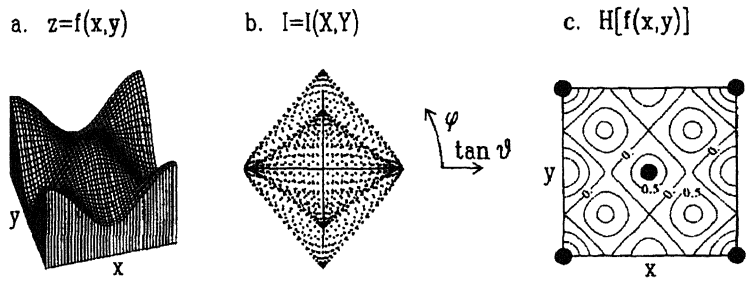

Fig. 3. Results of a reflection calculation from a periodical, corrugated hard wall, described by height function $z=f(x, y)=0.1(\cos x+0.25)\cos y$. The following plots are drawn (see also caption of fig. 2): (a) a 3-dimensional view of the hard wall surface as a function of (x, y); (b) the reflection pattern on the detection screen, showing the intensity distribution $I=I(X, Y)$; (c) a topographical plot of the corresponding Hessian as a function of (x, y).

contours are the lines $y=\pm x+(k+\frac{1}{2})\pi$, $k=0, \pm 1, \ldots$. The images of these lines under the mapping defined by eq. (16) are precisely the slightly curved sides of the "square" in fig. 2b. So these sides are indeed caustics. The four corners in the caustic are hyperbolic umbilics with $\Gamma=4A^4$, as follows from table 1. They are produced by the intersections of the zero-contours at $(m\pi/2, (m+2k+1)\pi/2)$, $m, k=0, \pm 1, \ldots$.

This example has a high order of symmetry. In addition to the reflection symmetry with respect to the lines $x=k\pi$ and $y=k\pi$, $k=0, \pm 1, \ldots$, which is shared by all members of the family of eq. (36), there is also a reflection symmetry with respect to the lines $x=\pm y$ (which pertains to all members of the family for which $p=q$) and an antisymmetry of f for reflection in the lines $x=(k+1/2)\pi$ and $y=(k+1/2)\pi$, $k=0, \pm 1, \ldots$. This antisymmetry is typical for the case $p=q=0$. Because of that, in this case f is periodic in the diagonal directions, too, with the period $\pi\sqrt{2}$. The simple shape of the caustic, in comparison with the examples to be discussed later on, is due to this additional periodicity.

For this particular example it is instructive to indicate the connection with the deflection functions. According to eq. (2) and ref. [4] reflection can be described using a double differential cross section $\sigma=\sigma(\vartheta, \varphi)$, where the deflection functions are $\vartheta=\vartheta(x, y)$ and $\varphi=\varphi(x, y)$. In most cases the deflection functions cannot be calculated analytically in a scattering process, but sometimes they can be computed numerically. But, in case of reflection, the final angles ϑ and φ are fully determined by the geometry of the surface (see eqs. (4) and (5)). For the case $p=q=0$ in eq. (36) they are shown in contour representation in figs. 2d and 2e (the dotted curves represent the zero-contour of the Hessian). The umbilics originate from impact points on the surface where ϑ and φ are extremal, which give focusing of particles in that specific direction (ϑ_0, φ_0). In between the umbilic impact parameters the zero-contour of H moves through saddle points in ϑ while φ changes monotonously.

The special symmetry discussed above is broken, at least partially, if we choose, for instance, p to be different from zero, while keeping $q=0$. This is demonstrated in fig. 3 where the results are shown for the case $p=0.25$ and $q=0$. The zero-contours, which were straight lines when p was zero, are now transformed into curved lines that meander in symmetric pairs around the vertical lines $x=0$ and $x=\pi$, as can be seen in fig. 3c. The symmetry with respect to the line $x=\pi/2$ is lost, but the one with respect to $y=\pi/2$ is retained. The reflection pattern has changed markedly as well. In addition to the caustic at the boundary of the pattern we see in fig. 3b a second caustic lying more inward. The two umbilics on the X-axis have disappeared. That is related to the fact that the zero-contours no longer intersect at $(\pi/2, \pi)$ and $(3\pi/2, \pi)$. Instead we now see two cusps in the inner caustic near the points where the outer caustic crosses the X-axis as a smooth curve. As we have mentioned before in section 3, this is the typical way in which the hyperbolic umbilic unfolds under perturbation.

The two umbilics which were present on the Y-axis in fig. 2b (where $p=q=0$) have each split into a pair of hyperbolic umbilics, which show up as corners in the outer and inner caustics on the Y-axis. This is in accordance with table 1. The diagonal symmetry is lost, because f is no longer invariant for the interchange of x and y if $p\neq 0$.

The pattern changes gradually when p is increased, although the main features remain intact, at least as long as $0<p<1$. In order to explain this we write down explicitly the equation for the zero-contour. From eq. (40) we find that for $q=0$ the solution of $H=0$ can be written as:

$$\cos y=\pm\frac{\sin x}{\sqrt{1+p\cos x}}. \tag{41}$$

This equation makes sense only when its right-hand side is in the range $[-1, 1]$. Therefore only those values of x are allowed for which either $|x|\leqslant\pi/2$ or $|\pi-x|\leqslant\arccos p$, if $0<p<1$. The pair of zero-contours lying in the strip $|x|\leqslant\pi/2$ produces the outer caustics, while the pair in the strip $|\pi-x|\leqslant\arccos p$ produces the inner caustic. The points $(0, \pi/2)$ and $(\pi, \pi/2)$ where the zero-contours intersect produce the hyperbolic umbilics.

Also of interest are the intersections of the zero-contours around $x=\pi$ with the lines $y=0$ and $y=\pi$. As an example, take the point $(x_1, 0)$, where $x_1=\arccos(-p)$. This point lies on the zero-contour, which is vertical there, because $\partial H/\partial y=0$, while $\partial H/\partial x\neq 0$ at $(x_1, 0)$. Hence, along the zero-contour (where $dH=0$) dx is equal

to 0 at that point. From eq. (38) we obtain $f_{xy}=A\sin x_1 \sin 0=0$ and $f_{yy}=-A(p+\cos x_1)\cos 0=0$. Therefore $\boldsymbol{j}\cdot d\boldsymbol{r}=f_{xx}dx+f_{xy}dy=f_{xy}dx+f_{yy}dy=0$ at $(x_1, 0)$. In section 3 (cf. eq. (30)) we have shown that this is the condition for a cusp (note that since $f_{xx}=-\cos x_1 \cos 0=p\neq 0$ this point is not an umbilic). From eq. (37) we find that $f_x=-A(1-p^2)^{1/2}$, $f_y=0$ for this cusp point, so that it lies on the X-axis if $|p|\leqslant 1$. The same result is obtained for the points $(2\pi-x_1, \pi)$, (x_1, π) and $(2\pi-x_1, 0)$, except that the last two points belong to the cusp points with $f_x=A(1-p^2)^{1/2}$, $f_y=0$.

At the points $(\pi/2, 0)$ and $(3\pi/2, 0)$ the zero-contours around the line $x=0$ cross the lines $y=0$ and $y=\pi$ vertically, as well, but at these points $|f_{yy}|=p\neq 0$, so that $\boldsymbol{j}\cdot d\boldsymbol{r}\neq 0$. These points, therefore, do not produce a cusp point. At their image points on the screen the outer caustic is a smooth curve, which meets the X-axis at a right angle.

From the data given above, we can now easily deduce what happens when the value of p increases from 0 to 1 while $q=0$ and A is kept constant. The shape of the zero-contour around $x=0$, where the outer caustic curve on the screen originates from, cannot change very much, because the position of the intersections with the lines $x=0$, $y=0$ and $y=\pi$ does not change with p. The zero-contours around the line $x=\pi$, however, are compressed towards this line because $\arccos p$ goes to zero as $p\to 1$. As a consequence the inner caustic shrinks. Both the umbilics at the X-axis and the cusps at the Y-axis converge to the origin, the cusps moving more slowly. In contrast, the hyperbolic umbilic at the top and at the bottom of the outer caustic, for which $f_x=0, f_y=\pm A(1+p)$, move outward as p increases. Since the intersections with the X-axis remain at the same place (for these $f_x=\pm A$, $f_y=0$), the outer caustic becomes more elongated in the Y-direction. That can be seen very clearly if we compare the reflection pattern in fig. 3b, where $p=0.25$, $q=0$, with the pattern in fig. 4a belonging to $p=0.5$, $q=0$.

In fig. 4 we have put together the different types of reflection patterns that can occur when p and q are changed. In each row the value of q is constant, while the value of p increases from left to right, as is indicated. In a column p is constant, while q increases in the downward direction. The amplitude A changes with p. We have set $A=0.1/(1+p)$ in order to keep the vertical dimension of the reflection pattern constant.

The reflection pattern for $p=1$, $q=0$ is shown in fig. 4b. The inner caustic has even shrunk further. In this particular case the Hessian can be factorized into:

$$H[f]=A^2(\cos x-\sin^2 y)(1+\cos x)\,. \tag{42}$$

From this it follows that one pair of the zero-contours has become a double line that coincides with $x=\pi$. The corresponding inner caustic is reduced to a single point lying at the origin of the screen coordinates. Table 1 tells us that this isolated caustic point is a parabolic umbilic ($\Gamma=0$). It shows up in fig. 4b as an oblong dark spot in the centre, stretched along the X-axis. The outer caustic is elongated in the other direction. It is now twice as small along the X-axis as it is along the Y-axis. It still contains two corners on the Y-axis, which are hyperbolic umbilics with $\Gamma=8A^4$ (cf. table 1). This surface, therefore, produces both hyperbolic and parabolic umbilics.

When we go further and look at the case $p>1$, $q=0$ the zero-contours are still given by eq. (41). But for $p>1$ this equation makes sense only if $|x|\leqslant \pi/2$ or $x=\pi$. Consequently, the zero-contours consist of a pair of curves meandering around the y-axis and the isolated points $(\pi, \pi/2)$ and $(\pi, 3\pi/2)$. With these isolated points correspond two isolated caustic points on the screen with positions given by $f_x=0, f_y=\pm A(p-1)$. From table 1 it follows that these caustic points are elliptic umbilics, because $\Gamma=4A^2(1-p)<0$ if $p>1$. In the reflection pattern they show up as dark spots on the Y-axis somewhat above and below the centre. The oscillatory pair of zero-contours produces the caustic at the boundary of the reflection pattern, which still has two sharp corners in it, the hyperbolic umbilics at the Y-axis. The pattern in fig. 4c has become narrower in the X-direction than it already was in fig. 4b.

Surveying the results obtained so far, we notice that the most striking changes have occurred in the inner region of the reflection pattern. That is due to the fact that the shape of the hard wall surface changes much more in the region around the line $x=\pi$, where the inner caustic is formed, than in the region around $x=0$, where the outer caustic comes from. This can be seen, for instance, from the behaviour of the stationary points of f when p is varied. Restricting ourselves to the subsquare $0\leqslant x, y\leqslant \pi$, in accordance with our convention, we find that

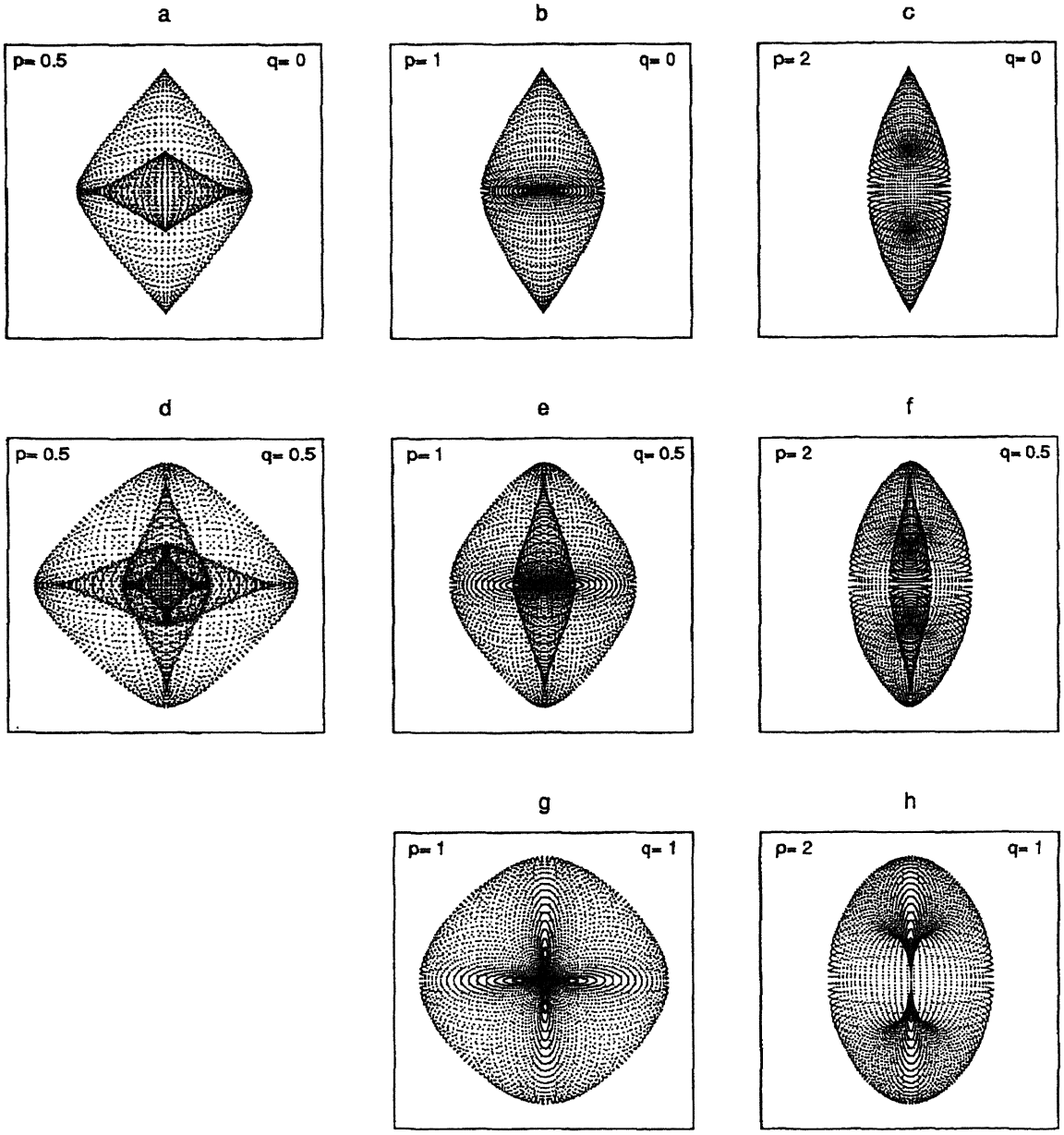

Fig. 4. Reflection patterns resulting from reflection by a periodical, corrugated hard wall described by the hard wall height function $z=f(x, y)=0.1\,(\cos x+p)\,(\cos y+q)/(1+p)$ calculated for various combinations of $p=0.5$, 1 or 2 and $q=0$, 0.5 and 1, as indicated in the light border.

for $0<p<1$, $q=0$ the hard wall surface has an absolute maximum equal to $A(p+1)$ at the point $(0,0)$, a local maximum $A(1-p)$ at (π,π), an absolute minimum of value $A(p-1)$ at $(\pi,0)$ and in between a saddle point at $(\arccos(-p), \pi/2)$ where $f=0$ (actually, $f=0$ along the whole line $x=\arccos(-p)$ and the whole line $y=\pi/2$). When p exceeds 1 the saddle point disappears, while the two extrema at $(\pi,0)$ and (π,π) turn into new saddle

points. Thus the landscape shows much more variation when $0<p<1$ (especially near the line $x=\pi$) then it does when $p>1$. The transformation of the pair of hyperbolic umbilics on the inner caustic via a parabolic umbilic into elliptic umbilics, when p passes 1, is connected with this radical change of shape of the surface near the line $x=\pi$.

We now turn to the cases where, in addition to p, the parameter q is different from zero, as well. Fig. 5 shows the results for the parameter setting $p=q=0.5$. Although the shape of the reflecting surface has not changed much in comparison with the surface with $p=0.25$ and $q=0$ (cf. fig. 3), the zero-contours and the reflection pattern have changed considerably. This is due to the loss of the reflection symmetry with respect to the line $y=\pi/2$, which was still present in the cases with $q=0$. The contourplot of the Hessian in fig. 5c shows that the zero-contours are now closed curves around the points $(k\pi, m\pi)$ with $k, m=0, \pm 1, \ldots$. Since zero-contours do not intersect anymore the caustics contain no hyperbolic umbilics in accordance with table 1. The umbilics that were present at the top and the bottom end of the reflection pattern in fig. 3b for $p=0.25$ and $q=0$ are decomposed into a smooth outer caustic curve and a nearby cusp pointing towards it, as usual. The same has happened to the two hyperbolic umbilics in the inner caustic on the Y-axis, although that is less discernable in fig. 5b. Because of this decomposition the reflection pattern now has a much more complicated structure. A more detailed analysis shows that the outer caustic at the boundary of the reflection pattern, with all corners rounded off, is produced by the zero-contour around the point (0,0). The zero-contour around $(\pi,0)$ produces a caustic in the form of a horizontal lip with cusps at its extremities near the outer caustic on the X-axis. A similar, but vertical lip is produced by the zero-contour around $(0,\pi)$. The middle zero-contour around (π,π), finally, is responsible for the caustic in the centre of the reflection pattern, which has four cusps. The eight cusps on the X- and Y-axes correspond to the points (x_a, y_a) on the zero-contours for which either $\cos x_a=-p$ and $\sin y_a=0$ (for cusps on the X-axis) or $\sin x_a=0$ and $\cos y_a=-q$ (for cusps on the Y-axis). Since the zero-contours are horizontal or vertical at these points, it is again easily verified with the help of eq. (38), that $f_{xx}dx+f_{xy}dy=f_{xy}dx+f_{yy}dy=0$ at (x_a, y_a), so that the condition for the cusp (see eq. (30)) is satisfied.

The pictures shown in fig. 5 are typical for all surfaces with $0<p, q<1$, except that they are not symmetrical with respect to diagonals when $p\neq q$. If we keep q constant, while $0<q<1$, and let p increase towards 1, then both the horizontal lip and the four-cusped caustic contract towards the centre, more swiftly in the Y-direction than in the X-direction. On the other hand, the vertical lip and the outer caustic expand in the Y-direction.

For the special case $p=1$ the Hessian factorizes into

$$H[f]=A^2(1+\cos x)[(1+q\cos y)\cos x-\sin^2 y]\,. \tag{43}$$

If $0<q<1$ the zero-contours of H consist of the line $x=\pi$ and closed curves around the points (0,0) and $(0,\pi)$. The line $x=\pi$ reflects to an isolated caustic point at the origin of the screen coordinates. This point is a parabolic umbilic, as can be inferred from table 1. In the reflection pattern of fig. 4e it shows up as an oblong concentration of dots in the centre, stretched along the X-axis. It strongly resembles the oblong spot in fig. 4b ($p=1$, $q=0$),

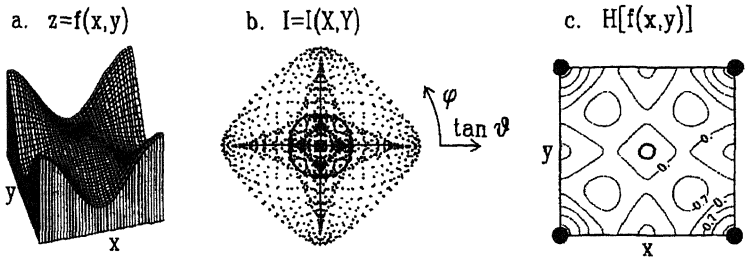

Fig. 5. Results of a reflection calculation from a periodical, corrugated hard wall, described by the height function $z=f(x, y)=0.1(\cos x+0.5)(\cos y+0.5)$. The following plots are drawn (see also caption of fig. 2): (a) a 3-dimensional view of the hard wall surface as a function of (x, y); (b) the reflection pattern on the detection screen, showing the intensity distribution $I=I(X, Y)$; (c) a topographical plot of the corresponding Hessian as a function of (x, y).

which was a parabolic umbilic, too. The outer caustic at the boundary of the reflection pattern and the inner vertical lip with cusps at its ends are produced by the zero-contours around (0,0) and $(0,\pi)$, respectively.

A new phenomenon occurs when $p>1$ and $0<q<1$. This can be seen in fig. 4f for the case $p=2$, $q=0.5$. There two triangular shaped dark spots appear inside the vertical lip at the Y-axis above and below the centre, each with one vertex pointing in the direction of the centre. The vertices of these "triangles" are actually cusps. This example may be considered as a perturbation of the case $p=2$, $q=0$ shown in fig. 4c. The cusped "triangles" are the typical unfoldings of an elliptic umbilic.

If, for a change, we keep p constant (with $p>1$), and let q increase, then the vertical lip shrinks towards the centre, while the cusped "triangles" grow. When q attains the value 1 the lip has been reduced to a single point at the centre of the reflection pattern. It has become a parabolic umbilic again. The two cusped "triangles" have grown so much that now they meet at the centre. An example is shown in fig. 4h for the case $p=2$, $q=1$.

When we make $q>1$, while still keeping p constant ($p>1$), the two cusped "triangles" merge into a pillow-shaped figure with four cusps. It is shown in fig. 6 in its most symmetrical form for the case $p=q=2$. In this case the Hessian can again be factorized:

$$H[f]=A^2(2\cos x\cos y+\cos x+\cos y-1)(\cos x+\cos y+1)\,. \tag{44}$$

The first factor corresponds to the zero-contour around the point (0,0) shown in fig. 6c. This contour produces, as usual, the outer caustic at the boundary of the reflection pattern in fig. 6b, which is now almost a circle. The last factor corresponds to the zero-contour around (π,π), which is responsible for the cusped pillow. The cusps correspond to the points (x_a, y_a) where $\cos x_a=\cos y_a=-0.5$. As an example take $(x_a, y_a)=(2\pi/3, 2\pi/3)$. At

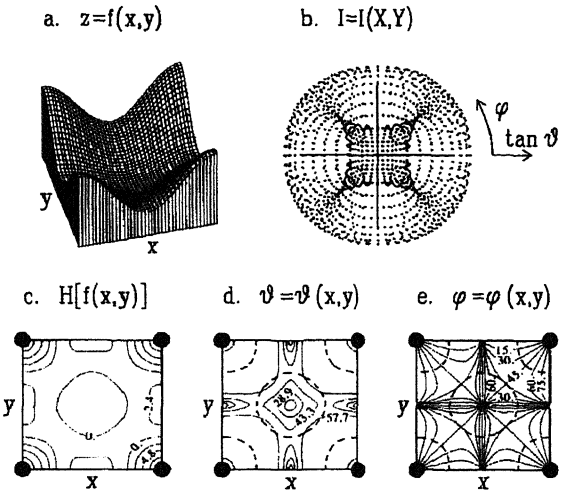

Fig. 6. Results of a reflection calculation from a periodical, corrugated hard wall, described by the hard wall height function $z=f(x, y)=0.1(\cos x+2)(\cos y+2)$. The following plots are drawn (see also caption of fig. 2): (a) a 3-dimensional view of the hard wall surface as a function of (x, y); (b) the reflection pattern on the detection screen, showing the intensity distribution $I=I(X, Y)$; (c) a topographical plot of the corresponding Hessian as a function of (x, y); (d) a topographical plot of the polar angle ϑ as a function of (x, y); (e) a topographical plot of the azimuthal angle φ as a function of (x, y).

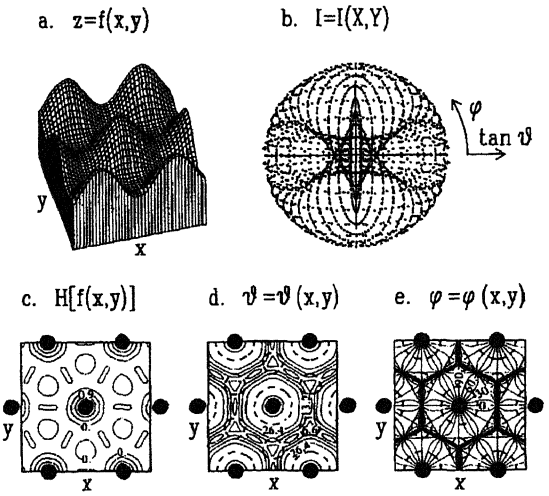

Fig. 7. Results of a reflection calculation from a periodical, corrugated hard wall, described by the height function $z=f(x, y)=\Sigma\exp[-(x-x_i)^2-(y-y_i)^2]$, $i=1, m$, where m is larger than 13. The following plots are drawn (see also caption of fig. 2): (a) a 3-dimensional view of the hard wall surface as a function of (x, y); (b) the reflection pattern on the detection screen, showing the intensity distribution $I=I(X, Y)$; (c) a topographical plot of the corresponding Hessian as a function of (x, y); (d) a topographical plot of the polar angle ϑ as a function of (x, y); (e) a topographical plot of the azimuthal angle φ as a function of (x, y).

this point $dx=-dy$ along the zero-contour, because this contour is symmetric with respect to the line $x=y$. From eq. (38) we find that $f_{xx}=f_{xy}=f_{yy}=0.75A^2$ at that point. Thus, we have indeed $\boldsymbol{j}\cdot d\boldsymbol{r}=0$ as required by the cusp condition in eq. (35).

Again we have plotted the contour plots of the deflection function $\vartheta=\vartheta(x,y)$ and $\varphi=\varphi(x,y)$ with the dotted curve representing $H=0$ laid over them. The outer caustic, a set of fold catastrophes, originates from a region around the (imaginary) atoms in the unit mesh where ϑ reaches a maximum (like a classical, one-dimensional rainbow) and φ changes monotonously. The original impact parameters producing the cusp catastrophes in the inner caustic on the screen coincide with broad saddle points in φ and local maxima in ϑ: the saddle point in φ takes care of the focusing of the particles at one spot on the screen, while the local maximum in ϑ is responsible for the typical vertex of the cusp at the same spot on the screen. These, more intuitively based arguments have already extensively been discussed in related studies (see refs. [18,23,24] and partly ref. [4]).

As a last example, we consider the case $p=q=1$, where the Hessian can be factorized as:

$$H[f]=A^2(1+\cos x)(1+\cos y)(\cos x+\cos y-1)\,. \tag{45}$$

The zero-contours now consist of a closed curve around the point (0,0), corresponding to the last factor, and the lines $x=\pi$ and $y=\pi$. The point (π,π) where the two lines intersect is very special. It turns out that in this point f and its derivatives up to and including third order all vanish. From the fourth derivatives only $f_{xxyy}=4A^2$ is different from zero. As a consequence the corresponding caustic, which is concentrated in the origin of the screen, is a catastrophe of even higher order than an umbilic. It shows up as a dark cross in the centre of the reflection pattern in fig. 4g with its arms along the X- and Y-axis.

The last part of this section is meant to demonstrate the influence of the surface geometry on the geometrical appearance of catastrophes. In this context, the surface geometry is particularly dominated by the symmetry of its unit cell, as we can see in the following calculation. Therefore, we will build up a periodical crystal lattice with atoms represented by Gaussians. Extra symmetry can then be created by changing the lattice structure, e.g., from a square to a hexagonal unit cell.

The hard wall and corresponding reflection pattern for a square unit cell are virtually identical to those of the cosine function shown in fig. 6. It suggests that taking this sum of Gaussians to construct a surface with a particular geometry is equivalent with the use of sinewave surfaces as an approximation of a crystal surface. The advantage of a construction using Gaussians is the flexibility in the geometry, whereas sinewave surfaces are restricted to certain symmetric geometries.

When we compare fig. 6 with the results for a hexagonal symmetry (in fig. 7) it is clear that although the same outer curve of folds is calculated, six cusps and corresponding saddle points in φ appear. This is simply due to the change in symmetry: from a 4-fold (square) to a 6-fold (hexagonal) symmetry. In fact, in case of the hexagonal symmetry, we have to deal with two times three connected cusps, reflecting the two equilateral triangles. So, the conclusion can be drawn that in those reflection calculations the number of observed cusps is essentially determined by the order of symmetry. These cusps originate from the center of the unit cell, which is obviously far more sensitive to this symmetry, in contrast to the regions around the atoms, from where the outer caustic curve originates. By contrast, for hyperthermal atom–surface scattering it has already been shown experimentally that the outer caustic curve is extremely sensitive to the symmetry of the unit cell, as a consequence of focusing and blocking effects due to multiple collisions, while structures from the middle of the unit cell are mostly too complex to analyze [23,24].

Summarizing, we have seen that there is a direct relationship between the occurrence of catastrophes and important features of the hard wall height function. Relevant information can be obtained from the order of observed catastrophes, their number and their geometrical appearance. In case of scattering from surfaces, this catastrophe analysis can be used as a tool to probe the local topology of the energy hypersurface.

5. Applications of catastrophe analysis

In section 4 it has clearly been demonstrated that catastrophes in reflection patterns can provide detailed information about the hard wall where the reflection took place. For surface scattering the same type of argument has already extensively been explored for one particular type of catastrophe, namely a rainbow in atom–surface scattering [6,7,9,26–29]. In this section we will extend this idea and we will speculate about certain obvious applications of reflection from solid surfaces. Because extensive experimental results using catastrophe analysis have not been obtained so far, we will evade to compare this technique with competitive ones, like helium scattering, and low and medium energy ion scattering.

To explore the experimental feasibility, we recall the assumption of single collisions, which can be seen as the assumption that the projectile should feel a limited surface corrugation. This can be obtained by decreasing the energy of the projectile. But then, two physical processes can become dominant in the scattering, namely diffraction and trapping. Diffraction can easily mask the reflection pattern completely. The criterion of diffraction is fulfilled when the de Broglie wavelength of the projectile is on the order of the periodicity length of the crystal [30], which is essentially the length of the crystal unit cell. Close to caustics diffraction occurs at even shorter wavelength, see e.g. eq. (4.7) of ref. [18]. For metals, this periodicity length is typically several angstroms. Scattering of thermal He with an energy of 20 meV, where the wavelength is ≈ 1 Å, will certainly give rise to diffraction [31]. Increasing the energy or the mass of the projectile lowers this wavelength. Scattering of 63 meV Ne [32,33] with a wavelength of 0.4 Å from a Ni, Pd and LiF target shows both features in the scattering pattern: diffraction maxima superposed on a rainbow peak. A further increase of the energy or of the mass of the projectile will result in pure reflection without diffraction. Increasing the initial energy with one or two orders will result in projectiles probing a reasonable corrugated surface. Consequently, they will undergo multiple collisions with the target (see refs. [6,7], 12–100 eV K on W(110) and ref. [29], 20–70 eV Na on W(110)) or will even be implanted in the surface (see ref. [9], 10–100 eV Na and K on Ag(111)). At the same time, dependently on the mass ratio between projectile and surface atoms, they can loose a sizable fraction of their initial energy to the surface atoms during the successive collisions [6,7,9,28].

The second process, i.e. trapping, is due to a well in the potential, which is strongly dependent on the chosen system. Projectiles with an initial energy in the same order of the well depth will, after exchanging even a small amount of their energy, be trapped in this well. Consequently, they cannot escape anymore from the surface until desorption takes place. So, trapping will give rise to a loss of reflected intensity and subsequently deterioration of the surface. In addition, the enhanced energy transfer for such a system will also effect the scattering patterns of the directly scattered particles [34]. This is the case for Ar and O_2 scattering with an energy of 0.1 eV from a Ag(111) crystal [35]. Even though the de Broglie wavelength is equal to 0.2 Å, no pure rainbow scattering is seen.

An intermediate energy range has been probed recently by Spruit et al. [35] in scattering of 1 eV O_2 from Ag(111), where the onset of surface corrugation has been observed. In these experiments the energy is high enough to prevent trapping and the de Broglie wavelength of the projectiles (0.05 Å) is small enough to avoid diffraction. Experiments at these energies with azimuthal resolution should be able to detect catastrophes in the scattering pattern as well.

To stress the importance of the crystal surface symmetry in catastrophe analysis, we mention the work of Luchesse and Tully [36], who theoretically showed the use of rainbow scattering of very low energetic particles, to determine the amount of reconstruction on a Si(100) surface. Their calculated histograms show beautifully fold and higher order catastrophes. They also compared the simulated scattering with experimental data of diffractive He–Si scattering [37].

Another application is to check the presence of adsorbed atoms on a surface, which in general will increase the corrugation and consequently the size of the observed rainbow angle. A related phenomenon is the presence or formation of molecules on the surface. This will show up in the appearance of additional higher order catastrophes. An analogy can be found in the scattering of light through a glass plate with water vapour condensed on

it, giving rise to diffuse scattering. At a certain moment, when nucleation and formation of water droplets takes place, clearly sharp structures will suddenly show up in the scattering pattern [38,39].

Now, we have only considered systems where symmetry or at least surface structure is probed. In principle, the same holds for the reverse: the absence or loss of symmetry or surface structure. One recent experiment, where this process has been studied is surface melting [40]. In such experiment a well-defined symmetry gets lost and consequently, this will ruin the well-characterized catastrophes in the reflection pattern. Another possible experiment, where the process is partly symmetry breaking, is the order–disorder transition at a certain critical temperature. Taking an alloy of two pronounced different elements this abrupt change in surface structure will be clearly visible in the catastrophe picture.

6. Catastrophe analysis in hyperthermal atom–surface scattering including energy transfer

In this section, we will actually use the catastrophe analysis for the determination of the important features of the repulsive part of the interaction potential ($V > 10$ eV), probed in purely classical scattering measurements, including energy transfer to the solid.

In experiments of 35 eV K scattered at normal incidence from W(110) [6,7] an extra rainbow feature was observed. In their analysis the authors of ref. [8] showed that the origin of this extra peak can be understood by an extra repulsion felt by the projectile in the middle of the unit cell. Van den Hoek et al. [41] theoretically demonstrated that this phenomenon should be attributed to electronic charge rearrangements of the K/W(110) system during the approach of the K ion to the center of the unit cell. In reflection calculations it is possible to visualize such a repulsion by a small extra contribution in the middle of the unit cell to the surface in fig. 6. In fact, this is done by calculating the reflection from the general cosine surface in eq. (36) with $p=q=0.5$ (see fig. 5). The conclusion from these calculations is that indeed extra catastrophes can be expected at small ϑ values. These structures are extremely useful to test the applicability of a model interaction potential to describe interactions of the projectiles with several surface atoms at the same time. Furthermore, in ref. [9] it is clearly demonstrated that the presence and absence of particular catastrophes is an easy method to show the onset of trapping and implantation of the projectiles in atom–surface scattering. This is also used in ref. [42] concerning molecular adsorption.

A series of hyperthermal scattering experiments of several alkali ions from two different crystalline metal surfaces have been performed, in which many rainbows have been observed. The scattering systems studied are 12–100 eV K on W(110) [6,7], 20–40 eV Na on W(110) [28], and 10–100 eV Na or K on Ag(111) [9]. To describe and analyze the experimental results classical trajectory calculations have been used [8,9]. In those calculations an interaction potential was taken, which came out of a Hartree–Fock–Slater (HFS) linear combination of atomic orbitals (LCAO) calculation [41]. One remarkable result of the theoretical analysis of the abovementioned experiments was the occurrence of higher order singularities in the differential cross section. We will now demonstrate the occurrence of higher order catastrophes, in particular the hyperbolic umbilic, in this kind of experiments. Furthermore, we will, just like catastrophe analysis is aiming at, show the connection between the occurrence of the hyperbolic umbilics and the local topology of the potential energy surface of this particular system.

The first experimental observation of hyperbolic umbilic catastrophes in hyperthermal atom–surface scattering is presented in ref. [43]. In those experiments on the Na/Ag(111) system the catastrophes are detected in the double differential cross section $\sigma = \sigma(\vartheta, \varphi)$. By detecting the one-dimensional catastrophe curves one is able to observe the azimuthal dependence of the scattering yield. In this way the crystal orientation or the surface symmetry can be made visible. It is shown that the stability of the catastrophes is that high that the sharp structures of the hyperbolic umbilic catastrophes survive the averaging of the thermal motions of the target atoms, even at a crystal temperature of 575 K [43].

The deflection functions involved in the scattering processes discussed here are given by $\vartheta = \vartheta(x, y)$ and

$\varphi=\varphi(x, y)$, while $E'=E'(\vartheta, \varphi)$ [2]. Due to the dimensionality of the problem and Liouville's theorem a two-dimensional cloud of particles parallel to the xy-plane will by scattering be transformed into a two-dimensional hypersurface, which is embedded in the three-dimensional space [12]. In this part we will take, for convenience, the (x', y', p') phase space, where p' denotes the momentum of the projectile after scattering. The hypersurface is calculated at infinity, which requires normalized position coordinates $x'=x/C$ and $y'=y/C$ (see also eq. (15)), where the limit is taken for the distance of the detection screen C going to infinity. In the present calculations energy exchange from the projectile to the solid is present and the hypersurface will span a certain volume in this particular phase space. Just to get an idea on how the hypersurface for potential scattering will look like, fig. 8 shows three projections of such a hypersurface. This particular hypersurface corresponds to 13 eV Na scattering from Ag(111) at normal incidence and is calculated in the (x', y', p') phase space. This result is obtained by classical trajectory calculation using an interaction potential determined with the HFS/LCAO method. Simulations with similar potentials have been used successfully earlier for this type of scattering [9,42]. Illustrative in fig. 8 are the caustic curves indicating the presence of catastrophes and the several lobes indicating the branches in the differential cross section formed by multiple collisions [6–9]. The correspondence between this hypersurface and the one calculated for the scattering of 35 eV K from W(110) at normal incidence (see fig. 6 of ref. [23]) strongly suggests the trends to be general for scattering at hyperthermal energies.

To prove now that fig. 8 contains higher order catastrophes we are going to use the knowledge obtained from sections 2 and 3, which is derived for reflection from hard wall surfaces. To do so, we employ a trick to make the classical trajectory calculation data comparable to hard wall reflection. We theoretically consider the intensity distribution $I=I(\vartheta, \varphi)$, drawn in the $x'y'$ projection in fig. 8, as resulting from a hard wall reflection calcu-

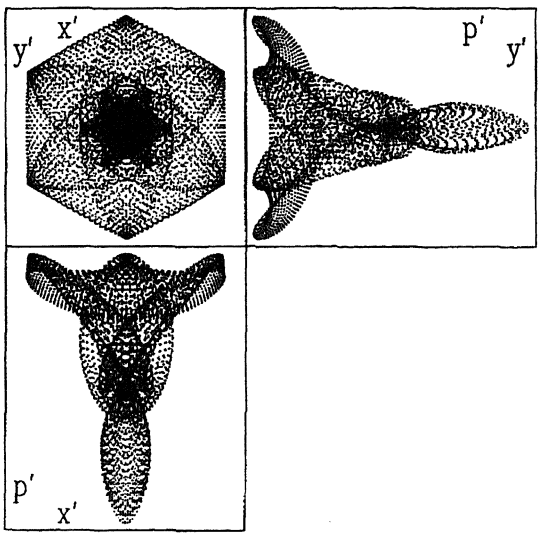

Fig. 8. Three projections of the calculated two-dimensional hypersurface after scattering of a cloud of 13 eV Na atoms at normal incidence from Ag(111). The hypersurface in the (x', y', p')-space is simulated with a classical trajectory calculation using an interaction potential determined via the HFS/LCAO method [9].

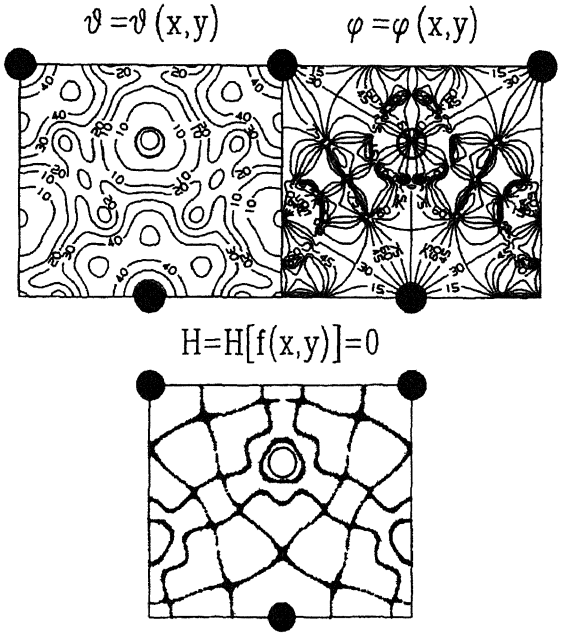

Fig. 9. Contour maps for the deflection functions $\vartheta=\vartheta(x, y)$ and $\varphi=\varphi(x, y)$, and the calculated Hessian curves $|H|=|H[f(x, y)]|<\epsilon_H$ as a function of the 2-dimensional impact parameter $b=b(x, y)$ for scattering of 13 eV Na at normal incidence from Ag(111). The same simulated data has been used as in fig. 8.

lation. This can be done because the deflection functions $\vartheta=\vartheta(x, y)$ and $\varphi=\varphi(x, y)$ from the simulations are smooth. In other words, we construct an "imaginary" hard wall reflecting surface which in a reflection calculation will give the same results for the intensity distribution $I=I(\vartheta, \varphi)$ as a function of the final angles. Of course, the energy transfer, characteristic for this hyperthermal scattering, is discarded in the construction of the reflecting surface: by this method only the projection of the hypersurface onto the (x', y')-plane is reconstructed. Discontinuous effects, like implantation or trapping of the projectiles at certain regions in the unit cell [9], give rise to sharp discontinuities in the "imaginary" hard wall surface, like sharp edges. This problem can be avoided by only taking into account the reflective parts of the unit cell. The "imaginary" hard wall surface will be much bumpier than the reflection examples in section 4, to account for the presence of multiple collisions in the scattering process, but it is without any irregularity.

From the deflection functions $\vartheta=\vartheta(x, y)$ and $\varphi=\varphi(x, y)$ the derivatives of the "imaginary" hard wall function $z=f(x, y)$ can be extracted as a function of x and y. The functions f_x and f_y can simply be calculated from the geometrical formulae (see also eqs. (4) and (5) and fig. 1)

$$f_x=\tan\tfrac{1}{2}\vartheta\cos\varphi, \quad f_y=\tan\tfrac{1}{2}\vartheta\sin\varphi\,. \tag{46}$$

In our case, we can calculate the corresponding Hessian from the data of the classical trajectory calculations by numerical differentiation of f_x and f_y with respect to x and y, using the simple formulae $f_{xx}=[f_x(x+h, y)-f_x(x-h, y)]/2h$ and so on. Subsequently, we are able to determine the zero-contours $r=r(t)=(x(t), y(t))$ of the Hessian numerically by imposing the condition $|H|<\epsilon_H$ with ϵ_H small. In this way we have found all impact parameters (x_i, y_i) on the surface unit cell which give rise to catastrophes in the scattering pattern. The result is plotted in fig. 9. The curves observed in this figure are the origin curves introduced earlier.

As a test for the quality of the numerical differentiation we have used the absolute difference $|f_{xy}-f_{yx}|$, because for any smooth hard wall surface, which is continuously differentiable, f_{yx} is equal to f_{xy}. In the calculation this was actually the case within the precision of the differentiation. As a second check we also calculated the Jacobian $J=|\partial(\vartheta, \varphi)/\partial(x, y)|$ by numerical differentiation of the two deflection functions $\vartheta=\vartheta(x, y)$ and $\varphi=\varphi(x, y)$ with respect to x and y. The curves $|J|<\epsilon_J$ and $|H|<\epsilon_H$ are almost identical, which greatly supports the concept of the "imaginary" hard wall surface.

In fig. 9 three plots have been drawn: two contour maps of the final angles ϑ and φ as a function of x and y and a plot of the origin curves in the surface unit cell. When we project the origin curves on the plots of the deflection function $\vartheta=\vartheta(x, y)$ and $\varphi=\varphi(x, y)$, we notice the following cases:

(a) The origin curves pass areas where the deflection function ϑ is (locally) maximal.

(b) The origin curves sometimes intersect in regions where both deflection functions ϑ and φ are extremal.

(c) In between the impact parameters of cases (a) and (b) the contour lines of the two final angles ϑ and φ are parallel along the origin curves.

The relation between the origin curves and the behaviour of the deflection functions $\vartheta=\vartheta(x, y)$ and $\varphi=\varphi(x, y)$ is quite obvious in the abovementioned cases when we look to the consequences for the Jacobian $J_{2\times2}$ in the differential cross section. In case (a) both elements of the first column of the Jacobian vanish, i.e. $\vartheta_x=\vartheta_y=0$, giving rise to a vanishing Jacobian. Case (b) can be translated into four zero elements of the Jacobian: $\vartheta_x=\vartheta_y=\varphi_x=\varphi_y=0$, which makes the singularity in the double differential cross section of higher order. Finally, case (c) should be seen as a vanishing Jacobian due to the presence of dependent columns: $\lambda\vartheta+\mu\varphi=0$. These arguments confirm the importance of considering the extrema in the deflection functions $\vartheta=\vartheta(x, y)$ and $\varphi=\varphi(x, y)$, as was also concluded from the reflection calculations. The role of the maxima in the polar angle ϑ is, of course, consistent with the general definition of a rainbow.

We have seen that one-dimensional origin curves on the surface unit cell are related to the occurrence of catastrophes in the scattering pattern and we may look at the Hessian of the "imaginary" hard wall surface constructed to generate these origin curves (using eq. (46)). Now we make use of the catastrophe classification for hard wall reflection, as is derived in sections 2 and 3. We notice that the origin curves in fig. 9 sometimes

intersect under a finite angle, but in most parts they just seem to walk over the unit cell. In fact, careful analysis of these curves revealed that at these impact parameters either the polar angle ϑ meets a (local) maximum or the two final variables ϑ and φ have parallel contours. The latter can simply be translated in the fact that the derivatives of the two angles are locally equal to each other, giving rise to dependent columns in the Jacobian, but also in the Hessian. This can just be seen from the relationships in eqs. (46) between f_x, f_y and ϑ and φ. Examining the roots of the Hessian for impact parameters of case (a) or (c) we find that eq. (35a) is satisfied. This means that these parts of the origin curves correspond to the fold catastrophe.

Of more interest are the singularities which originate from the impact parameters at the intersections of the origin curves (case (b)). As was already stated these points coincide with (local) extrema in the final variables ϑ and φ, especially saddle points in φ. The focusing of the particles from these broad saddle points into one specific set of outgoing angles (ϑ_0, φ_0) was already argued to be the reason of the higher rainbow singularity in the scattering spectra in refs. [9,43]. Clearly, the coincidence of the two extrema in the final variables, whether absolutely or locally, will just cause the Jacobian to become zero as all four elements vanish. At the same time this holds true for the Hessian, as a consequence of vanishing double derivatives of the "imaginary" hard wall surface: $f_{xx}=f_{xy}=f_{yx}=f_{yy}=0$, i.e. eqs. (35a) and (35c) are satisfied. Hence we conclude that we then have to deal with the occurrence of umbilic catastrophes, or, at least, a two-dimensional section through the umbilic on the detection screen. In an earlier publication these higher order catastrophes in the scattering patterns were by mistake entangled with cusp catastrophes [24].

Still there are three types of umbilic catastrophes, namely the hyperbolic, parabolic and the elliptic ones. In this case even that question can relatively simple be answered when we keep regarding hard wall reflection from the "imaginary" surface. Locally, the condition $H=0$ for the occurrence of catastrophes has two real solutions: $r=r_1(t)$ and $r=r_2(t)$, where t is an arbitrary curve parameter. These solutions can be seen as curves in fig. 9 over the unit cell intersecting at that particular point where the umbilic originates from. The existence of two real solutions for the condition $H=0$ has in section 3 shown to be the proof for the occurrence of a hyperbolic umbilic catastrophe!

The shape of the cusps of the hyperbolic umbilic catastrophes is rather unusual. The corners in the reflection pattern might be an atypical appearance of the hyperbolic umbilic catastrophe [44]. This might be due to the fact that the symmetry of the problem is high, because normal incidence is taken. However, similar shapes for the hyperbolic umbilics have been seen for simulations of K scattering from W(110) [23]. In this case calculations for non-normal incidence have been performed. These do not show a drastic change in shape of the scattering patterns around the cusps.

From analysis of the contour maps of the deflection function $\vartheta=\vartheta(x, y)$ and $\varphi=\varphi(x, y)$ (see fig. 9 and ref. [9]) we are able to easily connect the occurrence of the hyperbolic umbilic catastrophes and specific scattering phenomena, namely focusing and blocking. Around a surface atom there will be a more or less circular origin curve giving rise to the minimum total scattering angle $\Theta=\pi-\vartheta$. When the corrugation of the surface as probed by the incoming projectile is that small that multiple collisions do hardly occur, this curve will indeed be of circular shape, as can be seen from the examples in section 4. Nevertheless, in scattering at hyperthermal energies multiple collisions play a prominent role and they bring an azimuthal dependence in this origin curve around a surface atom. At those φ-directions where a second surface atom is nearby, e.g., $\varphi=60°$ and 120°, the projectiles bouncing off from the first surface atom at a relatively high polar angle $\vartheta>50°$ will be blocked in their outgoing trajectory by this second surface atom. This blocking effect gives rise to bending backwards. Consequently, projectiles impinging on the surface at φ-directions just in between, like $\varphi=90°$, will feel a minimum blocking effect, and thus, they will end at a maximum polar angle ϑ. Moreover, at the same time, this minimal blocking effect by the two nearest neighbour surface atoms will cause focusing into this minimal blocking azimuthal direction: due to the two blocking effects the projectiles coming in at φ-planes nearby will be slightly pushed back until a balance in the blocking is obtained, which is just on this minimal blocking plane. In this way the extremum in the polar angle, i.e. an absolute maximum in ϑ, coincides with an extremum in the azimuthal angle, i.e. a saddle point in φ, giving rise to a higher order singularity. In this way the circular origin curve around

a surface atom is deformed into a curve with a hexagonal structure, reflecting the surface symmetry. So, the presence of hyperbolic umbilics is clearly related to specific scattering phenomena. For the impact parameters in the middle of the unit cell, where the two Hessians' zero-contours intersect, focusing is also made by multiple collision effects. The projectiles hitting the surface at these points undergo rather complex trajectories and we will not discuss them here.

The experimental observation of several caustic curves, mainly consisting of fold catastrophes and sometimes split up by a hyperbolic umbilic, is reported elsewhere for the system of normally incident Na scattered from Ag(111) with an initial energy of 35 eV [43].

7. Conclusions

Summarizing, we conclude that catastrophe analysis can be developed as a tool to categorize the topology of intensity distributions of scattered particles by the important features in the scattering patterns, namely catastrophes. The catastrophes originate from the singularities in the differential cross section.

Catastrophe analysis for reflection from massive hard walls, derived in sections 2 and 3, is purely based on first principles. This analysis is grounded on two main aspects of catastrophes in reflection from surfaces. The first aspect is the occurrence of certain types of catastrophes, which is determined by the shape of the reflecting hard wall surface itself. Secondly, we have demonstrated that the geometrical appearance of catastrophes is a good probe for the surface symmetry.

Calculating various examples of reflection from periodical hard wall surfaces, we have shown that catastrophe analysis is a sensitive technique in surface scattering, when diffraction does not dominate the reflection pattern and trapping nor energy transfer does take place. We also indicated some obvious applications thereof, like experiments to study the presence of adsorbates on surfaces or to measure the reconstruction of surfaces.

Finally we have made a classification of the types of catastrophes for 10–100 eV atomic scattering from metal crystalline surfaces, which is deduced from the fact that atom scattering at hyperthermal energies can be described equivalently in terms of hard wall reflection. The equivalence is mathematically introduced by regarding an "imaginary" hard wall surface as the reflective medium at which the scattering took place, producing the scattering data. In practice, we have used the deflection functions $\vartheta = \vartheta(x, y)$ and $\varphi = \varphi(x, y)$ from the classical trajectory calculations to obtain the Hessian of this "imaginary" surface. This gives the opportunity to simply translate the results of catastrophe analysis for hard wall reflection to the abovementioned atom–surface scattering. From experimental and simulated results of 10–100 eV Na and K at normal incidence from W(110) [6–8,23,27] and from Ag(111) [9] we conclude that in this case two catastrophes have been observed, namely the fold and the hyperbolic umbilic catastrophes. We have shown the origin of these catastrophes in terms of the dependence of the scattering angles on the two-dimensional impact parameter.

Acknowledgement

The authors like to acknowledge E.A. Gislason and N.H. Temme for stimulating discussions, P.J. van den Hoek for calculating the Na/Ag interaction potential, U. van Slooten for his help with the preparation of the manuscript and Professor Dr. J. Los for critical reading of the manuscript. We thank R. van der Horst for his help in the preparation of the figures. AWK enjoyed enlightening discussions with M.V. Berry and J.F. Nye. This work is part of the research program of the Stichting voor Fundamenteel Onderzoek der Materie (Foundation for Fundamental Research on Matter) and was made possible by financial support from the Nederlandse Organisatie voor Wetenschappelijk Onderzoek (Netherlands Organization for the Advancement of Research).

References

[1] R.G. Newton, Scattering Theory of Waves and Particles (McGraw-Hill, New York, 1966).
[2] T.C.M. Horn, A.W. Kleyn and E.A. Gislason, Chem. Phys. 127 (1988) 81.
[3] E.A. Gislason, Chem. Phys. Letters 42 (1976) 315.
[4] T.C.M. Horn, A.W. Kleyn and E.A. Gislason, J. Chem. Phys. 85 (1986) 7388.
[5] A.W. Kleyn, Comments At. Mol. Phys. 19 (1987) 133.
[6] A.D. Tenner, K.T. Gillen, T.C.M. Horn, J. Los and A.W. Kleyn, Phys. Rev. Letters 52 (1984) 2183.
[7] A.D. Tenner, K.T. Gillen, T.C.M. Horn, J. Los and A.W. Kleyn, Surface Sci. 172 (1986) 90.
[8] A.D. Tenner, K.T. Gillen, R.P. Saxon, D.E. Harrison Jr., T.C.M. Horn and A.W. Kleyn, Surface Sci. 172 (1986) 121.
[9] T.C.M. Horn, Pan Haochang, P.J. van den Hoek and A.W. Kleyn, Surface Sci. 201 (1988) 573.
[10] R. Thom, Structural Stability and Morphogenesis (Benjamin/Addison-Wesley, New York, 1975).
[11] E.C. Zeeman, Catastrophe Theory: Selected Papers (1972–1977) (Addison-Wesley, Reading, 1977).
[12] T. Poston and I.N. Stewart, Catastrophe Theory and its Applications (Pitman, London, 1978).
[13] J.N.L. Connor, Mol. Phys. 31 (1976) 33.
[14] F. Drepper, J. Phys. C 10 (1977) 3431.
[15] H.J. Korsch and F. Wolf, Comments At. Mol. Phys. 15 (1985) 139.
[16] T. Uzer, J.T. Muckerman and M.S. Child, Mol. Phys. 50 (1983) 1215.
[17] H. Trinkaus and F. Drepper, J. Phys. A 10 (1977) L11.
[18] M.V. Berry, J. Phys. A 8 (1975) 566.
[19] M.V. Berry and C. Upstill, Progress in Optics, Vol. 18, ed. E. Wolf (North-Holland, Amsterdam, 1980).
[20] M.V. Berry, Physics of Defects, Les Houches Session XXXV, ed. R. Balian (North-Holland, Amsterdam, 1980) course 7.
[21] N. Neskovic and B. Perovic, Phys. Rev. Letters 59 (1987) 308.
[22] N. Neskovic, Phys. Rev. B 33 (1986) 6030.
[23] T.C.M. Horn, A.D. Tenner, Pan Haochang and A.W. Kleyn, J. Electron Spectros. Related Phenomena 38 (1986) 81.
[24] T.C.M. Horn and A.W. Kleyn, Springer Series in Surface Sciences, Vol. 11. The Structure of Surfaces II, eds. J.F. van der Veen and M.A. van Hove (Springer, Berlin, 1988) p. 83.
[25] M.V. Berry and J.H. Hannay, J. Phys. A 10 (1977) 1809.
[26] J.D. McClure, J. Chem. Phys. 57 (1972) 2823.
[27] E. Hulpke and K. Mann, Surface Sci. 133 (1983) 171.
[28] A.D. Tenner, K.T. Gillen and A.W. Kleyn, Nucl. Instr. Meth. B 17 (1986) 108.
[29] T.C.M. Horn, Pan Haochang and A.W. Kleyn, J. Vac. Sci. Technol. A 5 (1987) 656.
[30] J.M. Cowley, Diffraction Physics (North-Holland, Amsterdam, 1975).
[31] G. Brusdeylins, R.B. Doak and J.P. Toennies, J. Chem. Phys. 75 (1981) 1784.
[32] K.H. Rieder and W. Stocker, Phys. Rev. Letters 52 (1984) 352.
[33] G. Boato, P. Cantini and L. Mattera, Surface Sci. 55 (1976) 141;
A.D. LeGrand and E.F. Greene, J. Chem. Phys. 84 (1986) 6483.
[34] J.A. Barker and D.J. Auerbach, Surface Sci. Rep. 4 (1981) 1.
[35] M.E.M. Spruit, E.W. Kuipers, M.G. Tenner, J. Kimman and A.W. Kleyn, J. Vac. Sci. Technol. A 5 (1987) 496;
M.E.M. Spruit, P.J. van den Hoek, E.W. Kuipers, F.H. Geuzebroek and A.W. Kleyn, Phys. Rev. B 39 (1989) 3915;
M.E.M. Spruit, P.J. van den Hoek, E.W. Kuipers, F.H. Geuzebroek and A.W. Kleyn, Surface Sci. 214 (1989) 591.
[36] R.R. Luchesse and J.C. Tully, Surface Sci 137 (1983) 570.
[37] M.J. Cardillo and G.E. Becker, Phys. Rev. B 21 (1980) 1497.
[38] P.L. Marston and E.H. Trinh, Nature 312 (1984) 529.
[39] J.F. Nye, Nature 312 (1984) 531.
[40] J.W.M. Frenken and J.F. van der Veen, Phys. Rev. Letters 54 (1985) 134.
[41] P.J. van den Hoek, A.D. Tenner, A.W. Kleyn and E.J. Baerends, Phys. Rev. B 34 (1986) 5030;
P.J. van den Hoek, A.W. Kleyn and E.J. Baerends, Comments At. Mol. Phys. 23 (1989) 93.
[42] D. Halstead and S. Holloway, J. Chem. Phys. 88 (1988) 7197.
[43] T.C.M. Horn, U. van Slooten and A.W. Kleyn, Chem. Phys. Letters 156 (1989) 623.
[44] J.B. Delos, J. Chem. Phys. 86 (1987) 425.